Journal of Organometallic Chemistry 896 (2019) 154–161

Contents lists available at ScienceDirect

Journal of Organometallic Chemistry

journal homepage: www.elsevier.com/locate/jorganchem

New olefin metathesis catalyst bearing *N*-mesitylimidazole and nitrate ligands – Synthesis, activity, and performance in aqueous media

Marta Malinowska [a, *], Mariana Kozlowska [b], Agnieszka Hryniewicka [a], Jacek W. Morzycki [a]

[a] Institute of Chemistry, University of Białystok, Ciołkowskiego Street 1K, 15-245, Białystok, Poland
[b] Institute of Nanotechnology, Karlsruhe Institute of Technology, Hermann-von-Helmholtz-Platz 1, 76344, Eggenstein-Leopoldshafen, Germany

ARTICLE INFO

Article history:
Received 10 May 2019
Received in revised form
10 June 2019
Accepted 14 June 2019
Available online 16 June 2019

Keywords:
Ruthenium catalyst
DFT calculations
Mechanism of activation
Metathesis

ABSTRACT

A new 18-electron ruthenium complex, where ruthenium catalytic center is coordinated with the *N*-mesitylimidazole and nitrate ligands, as well as *o*-isopropoxystyrene moiety, is reported. The synthesis and detailed characterization of the Ru complex, together with density functional theory calculations (DFT), are presented. The complex is air- and moisture-stable, although has weak catalytical activity in the model metathesis reactions. However, its activity increases upon the addition of an aqueous HCl 1 M solution. Activated Ru complex successfully promotes metathesis in organic solvents as well as in water, enabling efficient performance (even up to 100%) of the catalyst under environment-friendly conditions. The activation mechanism of the reported catalyst is supported by time-dependent DFT calculations and *ab initio* molecular dynamics simulations.

1. Introduction

Olefin metathesis is widely known as a useful and powerful tool in modern organic chemistry. It allows to construct of carbon-carbon double bonds in different compounds, *e.g.* macromolecules [1,2] or biologically active compounds [3–5], making their synthesis easier and more efficient. Despite the progress of metathesis methodology, no universal catalyst, effective in all types of reactions has been designed yet. Though there are a lot of known and effective ruthenium catalysts, *e.g.*, **1**–**8**, shown in Fig. 1, in most cases, they have some limitations, including lack of reactivity during the synthesis of tetrasubstituted olefins and poor *Z*/*E* stereocontrol. Despite the success achieved by Grubbs et al. [6–8], as well as Hoveyda and Schrock [9], in obtaining a *Z*-selective catalyst, there is still a need to develop stable, easy-to-use complexes. In the face of the expectations of modern green chemistry, there are ongoing studies on the improvement of the metathesis catalysts and their adaptation to new challenges. Following the trend of environment-friendly chemical transformations, new catalysts that can be efficiently used in the reactions carried out in aqueous media are produced [10] and are still sought after.

Another class of the metathesis catalysts is represented by the latent complexes, which have been developed in recent years [11–15]. They were found to be especially attractive in metathesis polymerization reaction [16], where high control over the ROMP processes significantly improves the synthesis. The latent catalysts can be activated either by chemical or physical factors. One of the most frequently used methods of their activation is thermal [17–21] as well as UV-light [22–25] initiation. At the same time, activation using Brönsted acids has been reported recently [26–28]. Here, the most widely used additive is HCl [29–32], but also TSMCl [11], TFA [33] or even Cu(I) salts [34,35] are known to be effective. In general, the role of Brönsted acid (*i.e.* HCl) is to induce the anionic ligand exchange for more active chloride ligand.

It also facilitates dissociation of a suitable ligand allowing a latent metathesis catalyst to enter the catalytic cycle [36]. In the case of *tert*-butoxycarbonyl-aminobenzylidene catalyst **8**, HCl plays a dual role: it activates the chelate ring by protonation of the nitrogen atom, and it prevents the re-coordination of PCy_3 [15].

To analyze the microscopic properties of the synthesized catalysts and to understand the underlying mechanisms of their activation, quantum mechanical calculations are most frequently used and have become an integral part of the characteristics of new ruthenium complexes. Over the last year, there were many publications in which calculations confirmed the results of experiments. Here, Density Functional Theory (DFT) calculations have emerged

* Corresponding author.
E-mail address: marta.terpilowska@gmail.com (M. Malinowska).

https://doi.org/10.1016/j.jorganchem.2019.06.018
0022-328X/

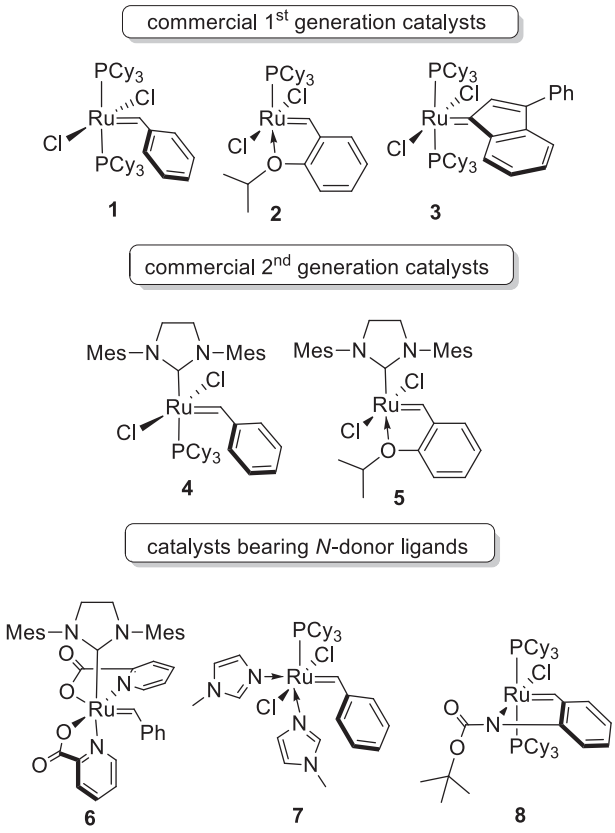

Fig. 1. Examples of ruthenium olefin metathesis catalysts. *Mes- 2,4,6-trimethylphenyl.*

as a valuable predictive tool to explain many aspects of Ru-catalyzed olefin metathesis. Jawiczuk et al. described the synthesis and DFT calculations of cationic carbenes [37], whereas Grela et al. proposed using DFT as reliable and accurate guidance in the fast and inexpensive design of new metathesis catalysts [38]. In another report from the group of Grela, DFT was used to optimize the geometry of new catalysts and the results led to a topographic steric map and calculation of percent 'buried' volume values for each quadrant around the metal center [39]. DFT calculations were also used to understand the influence of different ligand structures on the activity of a second-generation ruthenium olefin metathesis catalysts [40]. Many efforts have also been made to validate computational protocols. Kulkarni et al. assessed the performance of the DFT and Møller–Plesset second-order perturbation theory (MP2) to predict structural parameters in Ru complexes [41]. Zhao et al. discussed selected applications and validations of the Minnesota density functionals, focusing on catalysis [42,43]. Benitez et al. have used DFT with B3LYP and M06 functions to show factors responsible for diastereo- and enantioselectivity effects in the metathesis reaction [44]. Poater et al. used DFT calculations to rationalize the *Z*-selective catalyst mechanistic pathway [45] as well as to investigate the activation steps in various Ru-catalysts for olefin metathesis. Poater's group also proposed a computational protocol (M06/TZVP//BP86/SVP) for the Ru-based olefin metathesis catalysts [46]. The proposed method works with high precision, offering a computationally effective tool for rationalizing experimentally available data, as well as a prediction of the behavior of the catalyst.

In this paper, we report a novel protocol to obtain a new metathesis catalyst with the promising application in environment-friendly catalysis after acid activation. We synthesized the Ru complex containing *N*-mesitylimidazolium and nitrate ligands from Hoveyda 1st generation catalyst (**2**). The compound shows weak reactivity in model reactions, but after activation with aqueous 1 M HCl solution, the conversions increased to 92% (CH_2Cl_2, 40 °C) and to 100% (water, 40 °C). We studied the application profile of the catalyst in ring-closing metathesis (RCM), enyne cyclization and cross-metathesis (CM) reactions. In addition, we investigated in detail RCM of diethyl diallylmalonate in organic solvents, as well as in aqueous media. To gain insight into the activation mechanism of the new Ru catalyst, we performed the density functional theory calculations and *ab initio* molecular dynamics simulations. It should be underlined that the new catalyst can be obtained in efficient and straightforward two-step synthesis, it is easy to handle and may operate in aqueous media.

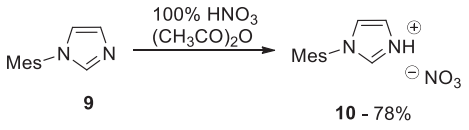

Scheme 1. Synthesis of imidazolium nitrate.

2. Results and discussion

The new latent catalyst was synthesized in two-steps: i) preparation of imidazolium nitrate; ii) reaction of the nitrate with base and catalyst **2**. The obtained new catalyst was characterized by NMR, IR, mass spectrometry and X-ray crystal analysis what is described in detail in the following subsections.

2.1. Synthesis

2.1.1. Synthesis of imidazolium nitrate

An imidazolium-based salt used in this study was prepared from *N*-mesitylimidazole (**9**) [47] by reaction with acetyl nitrate, generated *in situ* from fuming nitric acid and acetic anhydride. The reaction was carried out overnight and the volatile material was evaporated under a stream of nitrogen to obtain *N*-mesylimidazolium nitrate (**10**) in good yield (78%, Scheme 1).

2.1.2. Synthesis of new catalyst 11

The new catalyst was synthesized from the commercial complex **2** in the reaction with salt **10** and *t*-BuOK by stirring two hours in dry toluene at room temperature. The product was isolated by column chromatography as an air-stable crystalline green solid in 55% yield (Scheme 2). The possible mechanism the formation of the catalyst is shown on Scheme 3.

2.1.3. Characterization of new catalyst 11

The Ru complex **11** was characterized by NMR, IR, mass spectrometry and X-ray crystal analysis. The ^{1}H NMR spectrum of the catalyst **11** shows the characteristic signal for ruthenium carbene complexes at 19.51 ppm. There is also a singlet from the proton at C2 of the imidazole ring and signals derived from the phosphine

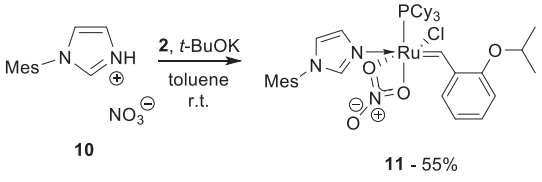

Scheme 2. Preparation of complex **11**.

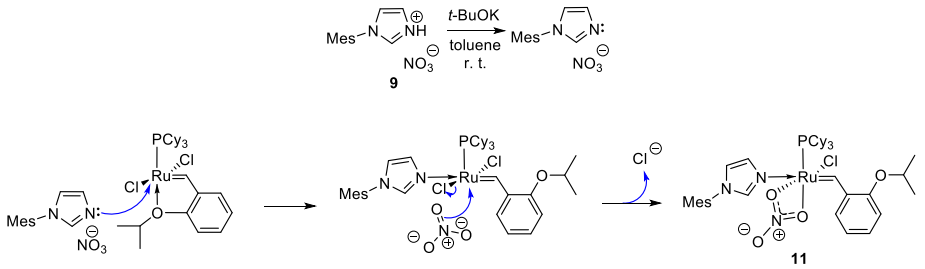

Scheme 3. The proposed mechanism of the catalyst formation.

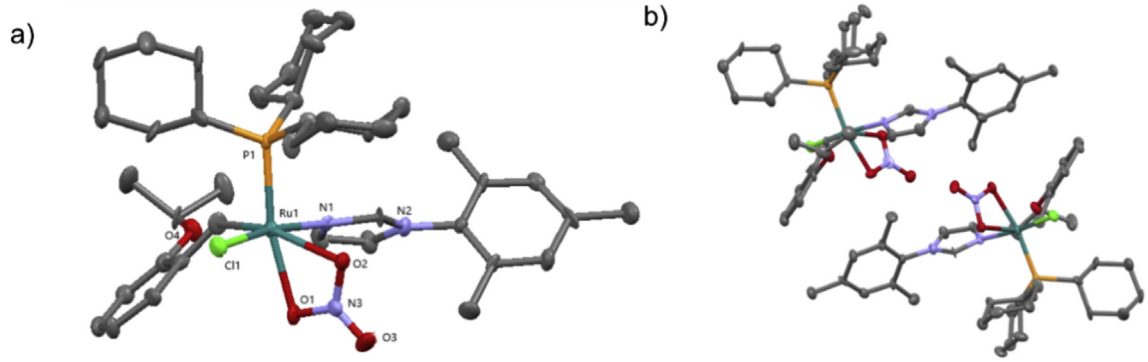

Fig. 2. The X-ray molecular structure of catalyst **11**. Hydrogen atoms were omitted for clarity (thermal ellipsoids are shown at the 50% probability level) a) single molecule b) dimer form of catalyst **11**.

ligand. The crystal structure of complex **11** is depicted in Fig. 2.

We estimated that the coordination geometry of the ruthenium center is triclinic: the ruthenium-oxygen coordination of the isopropoxy group is replaced by ruthenium-nitrogen coordination of *N*-mesitylimidazolium ligand. Additionally, one of the chlorine atoms is exchanged by bidentate nitrate ligand. The angle between the nitrogen atom of the imidazole ring and the bulky *o*-isopropoxystyrene ligand is 88°, and the nitrate group occupies an opposite position to the phosphine (Fig. 2). The X-ray analysis indicates that the complex **11** is prone to form dimers in its crystalline form.

In addition, the calculated molecular mass of catalyst **11** (813.2975) was not compatible with the observed ionic mass obtained from the MS-ESI spectrum (*m/z* found 761.3271). The difference in *m/z* value is triggered by the interaction between nitrate ligand and imidazolium ring, proceeding via leaving of Cl and OH radical, what is already known in the literature [48].

2.2. Performance of new Ru catalyst

The catalytic activity of the new catalyst was investigated in model RCM, CM, and enyne reactions and compared with that of the commercial 1st generation catalysts (**1**–**3**), as well as 2nd generation catalysts (**4**, **5**).

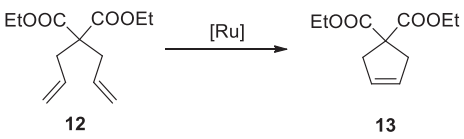

Scheme 4. Model RCM reaction of **12**.

2.2.1. The reaction rate of the ring-closing metathesis (RCM)

The RCM reaction of diethyl diallylmalonate (**12**, Scheme 4) was carried out in toluene (60 °C) or water (40 °C with SDS – sodium dodecylsulfate). The RCM reaction rate with catalyst **11** was followed by ^{1}H NMR and compared with that attained using complex **1**, which is shown in Fig. 3. Complex **11** initiates RCM significantly faster when reaction occurs in water in the presence of the surfactant than in toluene, despite lower reaction temperature.

2.2.2. Metathesis activity of complex *11*

Initial attempts to study the activity of **11** towards RCM under different conditions with and without an additive were focused on the cyclization of diethyl diallylmalonate (**12**). The reactions were

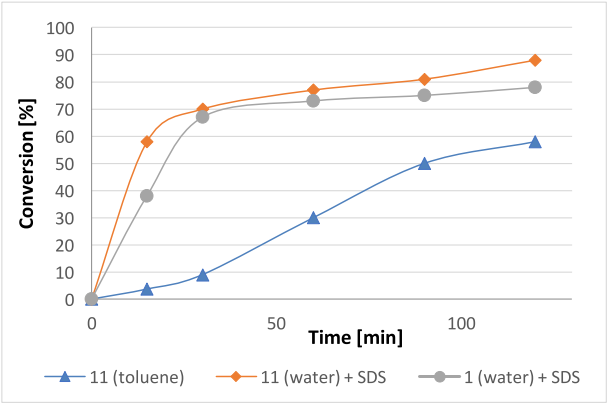

Fig. 3. RCM of diallylmalonate **12** with 5 mol% catalyst **11** or **1** at 40 °C (water)/60 °C (toluene). The conversion was determined by ^{1}H NMR spectroscopy.

Table 1
RCM of **12** with **11** with or without an additive[a].

Entry	Solvent	Temp.	Time	%mol **11**	Additive[b]	Yield[c]
1.	CH_2Cl_2	25 °C	2 h	1	–	6.5%
2.	CH_2Cl_2	40 °C	160 h	5	–	24%
3.	Toluene	60 °C	2 h	5	–	58%
4.[d]	Water	40 °C	16 h	5	–	32%
6.	CH_2Cl_2	40 °C	0.5 h	5	CuCl	10%
7.	CH_2Cl_2	40 °C	16 h	5	CuCl	66%
8.	CH_2Cl_2	40 °C	2 h	5	HCl	92%
9.	CH_2Cl_2	40 °C	2 h	5	TMSCl	72%
10.	CH_2Cl_2	40 °C	2 h	1	HCl	15%
11.	Toluene	60 °C	2 h	1	HCl	66%
12.	Toluene	60 °C	3 h	1	HCl	81%
13.[d]	Water	40 °C	2 h	5	HCl	100%

[a] Conditions: solvent (0.1 M), temperature, time, cat. **11**.
[b] $n_{additive}:n_{catalyst} = 10:1$.
[c] Determined by ^{1}H NMR.
[d] C = 0.17 M.

carried out in such solvents as CH_2Cl_2, toluene, and water at room temperature, 40 °C or 60 °C (Table 1). The catalyst has very weak activity at room temperature in CH_2Cl_2 (Table 1, entry 1), even at 60 °C in toluene the conversion was only 58% (Table 1, entry 3). The addition of CuCl, TMSCl (trimethylsilyl chloride) or the aqueous solution of 1 M HCl (10:1, $n_{additive}:n_{catalyst}$ each) causes the increase of obtained yields. Diethyl diallylmalonate (**12**) is fully converted into **13** after 2 h of reaction carried out with 5 mol% of catalyst **11** in water at 40 °C with the addition of 1 M HCl (Table 1, entry 13). After changing the solvent into CH_2Cl_2, the conversion of 92% is achieved (Table 1, entry 8). The conversion decreases to 81% in the presence of 1 mol% **11** after 3 h of reaction at 60 °C when the cyclization is performed in toluene (Table 1, entry 12). As it is discussed further, the activation results from the conversion of the 18-electron complex into the corresponding 14-electron benzylidene complex (Scheme 5).

The obtained results are very promising, especially the ability to react at low temperatures, which prevents unexpected thermal decomposition of the catalyst. Such high-temperature decompositions have been described by Grubbs et al. [49–51]. They have also been theoretically calculated by Cavallo and Nolan et al. [45,52,53]. It should be emphasized that metathesis carried out in primary alcohol solutions at elevated temperatures and prolonged reaction times may lead to the decomposition of ruthenium catalysts to a monohydride species [54,55]. The application of mild reaction conditions may protect the catalyst against these undesired transformations.

2.2.3. Metathesis in water with surfactants

The comparative study of catalysts **11** and commercial **1**–**5** in the RCM of **12** was carried out in water in the presence of surfactant

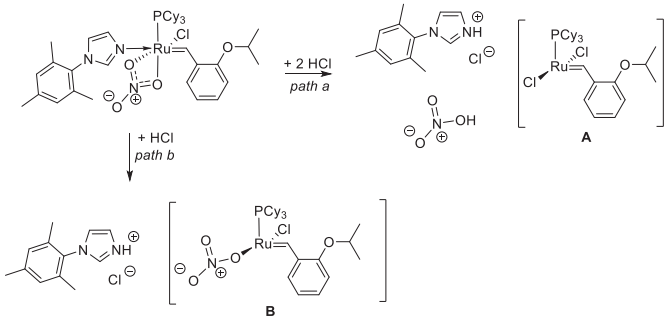

Scheme 5. Potential pathways of activation of complex **11** by HCl.

Table 2
Comparative study of catalysts in RCM of **12** in water[a].

Entry	Catalyst	Surfactant[b]	Yield[c]
1.	**11**	SDS	88%
2.	**1**	SDS	79%
3.	**2**	SDS	83%
4.	**3**	SDS	93%
5.	**4**	SDS	100%
6.	**5**	SDS	100%
7.	**11**	Tween 40	28%
8.	**1**	Tween 40	67%
9.	**2**	Tween 40	81%
10.	**3**	Tween 40	98%
11.	**4**	Tween 40	100%
12.	**5**	Tween 40	100%

[a] Conditions: water (C = 0.17 M), 40 °C, 2 h, 5 mol% [Ru].
[b] 0.2 equiv. (20 mol%).
[c] Determined by ^{1}H NMR.

Table 3
Comparative investigation of catalysts **1** and **11** in RCM.

Entry	Substrate	Product	Conditions	Catalyst	Yield[b]
1.	 12	 13	40 °C, 3 h, water, 0.17 M 5 mol% [Ru]	**11**[a] **1**	100% 53%
2.	 14	 15	40 °C, 3 h, CH_2Cl_2, 0.1 M 5 mol% [Ru]	**11**[a] **1**	18% 94%
3.	 16	 17	40 °C, 20 h, CH_2Cl_2, 0.1 M 5 mol% [Ru]	**11**[a] **1**	53% 100%
4.			40 °C, 3 h, water, 0.17 M 5 mol% [Ru]	**11**[a] **1**	36% 76%

[a] Catalyst **11** was used with 50 mol% $HCl_{(aq)}$ (1 M).
[b] Determined by ^{1}H NMR.

(SDS - sodium dodecylsulfate, Tween 40 – polyoxyethylene sorbitane monopalmitate) and is presented in Table 2. The complex **11** shows high activity (88% yield) in the presence of SDS as the surfactant in a ratio [substrate]/[SDS] = 5, comparable to that of commercial compound **1** (Table 2, entry 1 and 2). The increase in reaction rate is probably due to the formation of micelles. Unfortunately, Tween 40 has a less significant impact on the reaction yields (Table 2, entry 7).

2.2.4. Activity of complex *11* in model RCM, enyne and CM reactions

Catalysts **11** and **1** (5 mol%) were screened in a selected set of RCM, enyne and CM reactions. In all reactions with **11** aqueous 1 M solution of HCl was added (Tables 3 and 4). Diethyl diallylmalonate (**12**) was again subjected to cyclization in water to achieve full conversion using **11**, whereas the activity of **1** was two times lower (Table 3, entry 1). Diethyl methylallylmalonate (**14**) is more challenging in RCM than **12** due to steric effects, and only 18% yield was obtained for catalyst **11** (Table 3, entry 2). The RCM reactions of diethyl dimethylallylmalonate, leading to tetrasubstituted olefin using both complexes, failed. In the enyne cycloisomerization of **16** catalyzed by **1** in CH_2Cl_2 quantitative conversion was observed (Table 3, entry 3), whereas new complex **11** reacted with lower efficiency (53%). In the reaction conducted in water, again twice higher catalytic activity of **1** was observed as compared to **11** (Table 3, entry 4).

Next challenging reaction was the CM of allylbenzene (**18**) and *cis*-1,4-diacetoxy-2-butene (**19**). In this transformation, **11** gave only 12% conversion, which was significantly lower than that attained for **1** (Table 4, entry 1). The homodimerization reactions were

Table 4
Comparative investigation of catalysts **1** and **11** in CM reactions.

Entry	Substrate(s)	Product	Conditions	Catalyst	Yield[b]
1.	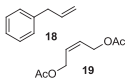	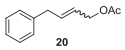	40 °C, 20 h, CH_2Cl_2, 0.1 M, 5 mol% [Ru]	**11**[a] **1**	12% (21% *Z*) 43% (22% *Z*)
2.		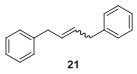	35 °C, 20 h THF, 3 M 5 mol% [Ru]	**11**[a] **1**	36% (45% *Z*) 59% (35% *Z*)
3.		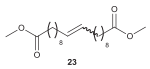	35 °C, 20 h THF, 3 M 5 mol% [Ru]	**11**[a] **1**	31% (54% *Z*) 33% (50% *Z*)

[a] Catalyst **11** was used with 50 mol% $HCl_{(aq)}$ (1 M).
[b] %*Z* determined by ^{1}H NMR, isolated yields after silica gel chromatography.

carried out at a relatively high substrate concentration (3 M). In homometathesis of **18**, catalyst **11** showed lower reactivity than **1** (Table 4, entry 2), but better *Z*-selectivity (45% of isomer *Z*). Finally, the activity of catalyst **11** was investigated for the homodimerization reaction of methyl 10-undecenoate (**22**) substrate. Comparative conversions for both catalysts were obtained. However, in the case of reported here complex **11**, relatively more *Z*-isomer was formed (Table 4, entry 3).

2.3. Activation mechanism

It can be seen from Table 1 that the product yield with catalyst **11** increases up to 92% and 100% upon the addition of HCl additive in CH_2Cl_2 and water, respectively. At the same time, we have noticed visual changes of the complex **11** after its HCl activation: the synthesized compound is green but acquires brown color in its active form (Fig. 4) that suggests a change of the chemical composition of the catalyst upon the addition of HCl. The ^{1}H NMR spectrum in deuterated chloroform in the presence of traces of acid shows additional carbene proton signals at 20.32 ppm and 18.79 ppm. It can, therefore, be inferred that a new Ru=CH species forms during the spectrum registration.

According to the literature [13], there are several potential pathways of activation of complex **11** by HCl. One possibility (*path a*) is that the acid protonates both imidazole and nitrate ligands, exchanging them for chloride to form a 14-electron benzylidene complex **A** (Scheme 5). In the *path b* only the imidazole ligand undergoes protonation, while the complex **B** with the nitrate ligand acts as an active catalyst.

To estimate the reason of the catalyst color change and to find the active form of the latent complex **11**, theoretical calculations, including density functional theory (DFT), time-dependent DFT (TD-DFT) and *ab initio* molecular dynamics (MD), were performed. Using the determined X-ray structure of the complex **11** (*see* Fig. 2), the gas-phase geometry optimizations of the dimer and monomer forms of the complex **11**, and also of complexes **A** and **B** (*see* Scheme 5), were performed using B3LYP functional with def2-SVP basis set as described in the section "Theoretical calculations". No significant structural differences between DFT optimized structures and their equivalent in the crystal were detected (*see Supporting Information*). The optimized structures were used in further investigations.

Due to the fact that it was not possible to measure the UV–vis spectra of the latent and active forms of **11**, we calculated the absorption spectra of all reactants with the TD-DFT approach. The first twenty singlet-singlet excitations of the monomer form of **11**, **A** and **B**, together with the first forty singlet-singlet excitations of the dimer form of **11**, are depicted in Fig. 5. Though the strongest excitations are localized in the UV region, several close-to-dark states in the visible region were detected (*see* the zoomed region in Fig. 5).

The transition orbitals and electron densities upon the most relevant excitations on the spectra are shown in Fig. S1 (*see Supporting Information*). Spectral changes in the visible region of all examined compounds clearly indicate that only the dimer form of complex **11**, as known from X-ray analysis, is green. The dimer of complex **11** absorbs in the violet and red regions and does not absorb green wavelength localized at ca. 500–570 nm, therefore, it is green. Upon the addition of HCl, the dimer of **11** transforms into the monomer form, which immediately undergoes protonation and activation with the simultaneous change of the color to brown. In Fig. 5, there are no absorption bands in the red region of complexes

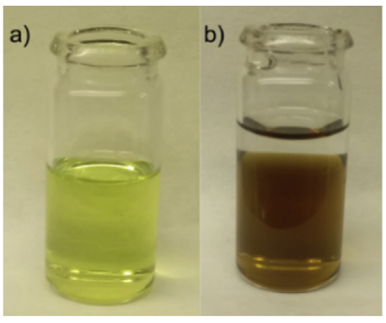

Fig. 4. The color change of the catalyst **11** solution in CH_2Cl_2 a) the inactive form b) the active form with the addition of 1 M aqueous HCl solution. (For interpretation of the references to color in this figure legend, the reader is referred to the Web version of this article.)

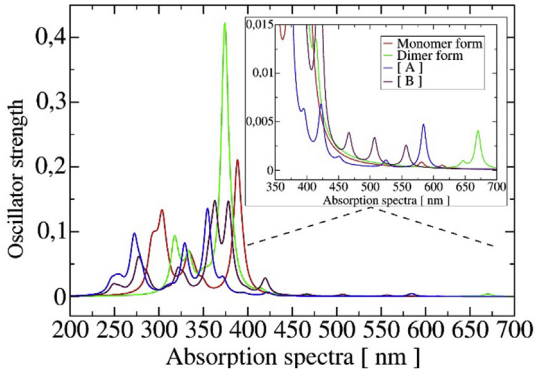

Fig. 5. Absorption spectra of monomer and dimer form of complex **11**, complexes **A** and **B**, as given in Scheme 5, obtained from the time-dependent DFT calculations with B3LYP functional and def2-SVP basis set.

A and **B**, but new bands in the green and close-to-green regions appear, what confirms the correctness of the assumptions presented in Scheme 5. The lack of the absorption bands at 670 nm and the dark states in the green region are characteristic to the monomer form of **11** (marked in red in Fig. 5), confirming the latent form of **11** as a dimer and change of the color upon dimer decay. Among the spectral changes there is also a 14 nm red-shift at 374 nm in the monomer of **11** in comparison to its dimer form.

After the detailed analysis of the transition orbitals upon the singlet excitations (listed in Tables S1–S4, *see Supporting Information*), we have found that the local environment of the complex **11** in its dimer form is different than in the monomer form. This influences the electron density localization on the frontier molecular orbitals, changing the respective orbital energies of the highest occupied molecular orbital (HOMO) and the lowest unoccupied molecular orbital (LUMO), inducing the mentioned shift. The energy of HOMO orbital of complex **11** changes from −4.976 eV in a monomer form to −4.985 eV in a dimer form of this complex, while LUMO energy changes from −1.779 eV to −1.946 eV. As it is shown in Fig. S2 (*see SupportingInformation*), the electron density transitions upon absorption occur from the metal center, imidazole and chloride ligands to *o*-isopropoxystyrene. In the dimer of complex **11**, there is close positioning of *N*-mesitylimidazolium ligand of one monomer to *o*-isopropoxystyrene of the other monomer and C-H···π interactions between these aromatic rings (*see* dark yellow surfaces in Fig. 6). These interactions together with the set of other intermolecular π-interactions and C-H···O hydrogen bonds (marked with black dashed lines in Fig. 6a) influence both the shift and the absorption bands in the red region. These intermolecular C-H···O hydrogen bonds are of the H···O distance of 2.31 Å and CHO angle of 128°, therefore, can be classified as weak H-bonds [56]. The qualitative analysis of the mentioned interactions was made using the noncovalent interaction (NCI) index utilizing NCIPLOT code (v.3.0) [57,58]. The obtained NCI surfaces are marked in dark yellow in Fig. 6. The binding energy of the NCI in the dimer of **11** was calculated as 38.1 kcal mol^{-1} using the supermolecular approach. It indicates strong intermolecular interactions in the dimer, therefore its high structural stability, differences in the absorption spectrum, and lower catalytic activity, specifically in the aqueous solutions. This form is catalytically less active because the metal active center is blocked for the desired reaction due to the hydrophobic nature of the outer dimer coating (*see* Fig. 6). As a result, firstly, the dimer of **11** should be broken to enable further catalyst activation due to the protonation. Upon the addition of HCl, all mentioned transitions occur easier; therefore, the significant increase in the activity of **11** is observed. This was also observed in *ab initio* MD simulations of the dimer of complex **11** with ten HCl molecules. Even if the time of the MD simulations was short (2 ps), we captured the formation of temporary interactions via Cl-H···O and Cl-H···N bridges (*see* snapshot 1, 3, 4 in Fig. S2 in *Supporting Information*), which participate during the protonation of nitrate and imidazole ligands.

Moreover, we monitored the bond breaking between both Ru-nitrate and Ru-imidazole, as depicted in snapshot 3 and 4 in Fig. S2 (*see Supporting Information*), respectively. Owing to the fact that NO_3^- ligand is smaller and more labile than *N*-mesitylimidazolium ligand, and the energy of its coordination to Ru is lower by 8.9 kcal mol^{-1} than that of imidazole: 46.1 kcal mol^{-1} and 55.0 kcal mol^{-1} for nitrate and imidazole, respectively, we assume that *path a* in Scheme 5 is more probable than *path b* at 0 K. Additionally, the coordination of the active center with chloride ligand in the complex **A** is 14.3 kcal mol^{-1} energetically more favorable than for the formation of the nitrate containing complex **B**.

To take into account the impact of all reagents during the activation of complex **11**, we calculated the reaction energy of proposed reaction paths (as shown in Scheme 5). The total free energy of the reaction in the *path a* and *b*, calculated with thermodynamic functions obtained from the vibrational spectra (*see* Table S5 in *Supporting Information*) using hybrid B3LYP functional with def2-SVP basis set, is +16.5 kcal mol^{-1} and +15.9 kcal mol^{-1} at room temperature and +16.2 kcal mol^{-1} and +15.5 kcal mol^{-1} at 40 °C, respectively. To estimate the impact of the DFT functional used in the calculated energy differences, we have performed similar calculations using meta-GGA functional, *i.e.*, TPSS functional [59], which has been shown before to give reliable values of reaction barriers [60]. Calculations with TPSS functional (*see* Table S6 in *SupportingInformation*) confirm small free energy differences between reactions proceeding according to the *path a* and *b*: free energies are in the range of +12.5 − +14.8 kcal mol^{-1} with the difference between two pathways of 1.6 kcal mol^{-1}. Here, the same as in the case of B3LYP functional, *path b* has lower reaction energy difference. This suggests that reactions according to the *path a* and *path b* both take place at room temperature (energy barriers are below 20 kcal mol^{-1}), but energy differences, *i.e.*, 0.65–0.67 kcal mol^{-1} and 1.58–1.61 kcal mol^{-1}, obtained with B3LYP and TPSS functionals, respectively, are lower than the accuracy of the DFT method. Therefore, they should be treated only qualitatively. More precise methods, like CCSD(T), should be used in this case, but taking into account amount of electrons of the examined molecular complexes and not realistically feasible calculation of force constants used in free energy calculations, we are limited in usage of this sophisticated method.

Based on the DFT calculated data, both reaction pathways in Scheme 5 are possible, but owing to higher coordination affinity of chloride ligand in comparison to the nitrate ligand, complex **B** is prone to change to complex **A**, where the latter is more stable

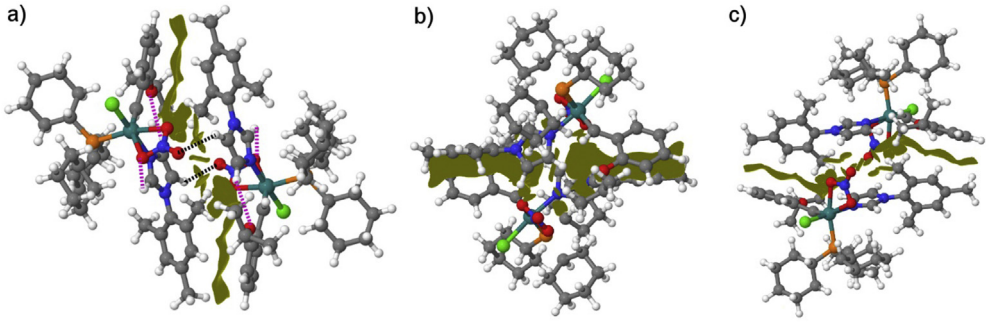

Fig. 6. Dimer form of the catalyst **11** with visualized intermolecular noncovalent interaction (NCI) regions, *i.e.*, π-interactions and C-H···O hydrogen bonds, from different perspectives (a, b, c). The depicted NCI surfaces correspond to the reduced density gradient of 0.4 a.u [57,58]. Intermolecular and intramolecular C-H···O H-bonds are marked with black and pink dashed lines in a), respectively. (For interpretation of the references to color in this figure legend, the reader is referred to the Web version of this article.)

complex. Therefore, we suggest that the active form of the catalyst **11**, reported here, is complex **A** (Scheme 5).

3. Conclusions

New metathesis catalyst with *N*-mesitylimidazolium and nitrate ligands was synthesized using the efficient and straightforward procedure as well as it was characterized by NMR, IR, MS and X-ray analyses. The catalytic activity of the Ru complex was tested under several reaction conditions, where the new catalyst in some cases showed better activity than commercially available 1st generation catalysts. The increase of yield up to 100% was observed in aqueous media upon the addition of 1 M HCl solution, which activates the catalyst. This activation under mild conditions allows to avoid undesired side reactions. The metathesis reactions carried out in aqueous media are environmentally friendly and advantageous from economical point of view.

The activation mechanism was proposed and confirmed with the density functional theory calculations and *ab initio* molecular dynamics simulations. It is based on the decay of the stable dimer of complex **11** in acidic conditions with further protonation of both imidazole and nitrate ligands by HCl, ligand exchange for chloride, and formation of an active 14-electron benzylidene complex. The absorption spectra of inactive and active forms of the catalyst were obtained with the time-dependent DFT calculations. A detailed analysis allowed to propose the active form of the Ru complex and to explain the reason of the color changes upon the activation of a catalyst. Free energy calculations, performed using B3LYP and TPSS functionals, confirm the occurrence of the suggested activation pathways and the most probable form of the active catalytic complex.

4. Materials and methods

4.1. Synthesis

4.1.1. General remarks

Synthesis of catalyst **11** was carried out using standard Schlenk techniques under an atmosphere of dry argon. CH_2Cl_2 was dried by distillation over CaH_2, THF over Na/benzophenone. Melting points were determined on an MP70 (Mettler Toledo) apparatus and were uncorrected. ^1H and ^{13}C NMR spectra were recorded on a Bruker Avance II spectrometer (400 and 100 MHz, respectively). Spectra are referenced relative to the chemical shift (δ) of TMS. Mass spectra were obtained with Micromass LCT TOF and Accurate-Mass Q-TOF LC/MS 6530 spectrometers. IR spectra were recorded on a Nicolet series II Magna-IR 550 FT-IR spectrometer. Column chromatography was performed on silica gel 230–400 mesh. Catalysts **1**–**5** are commercially available. Substrates for testing catalysts in RCM reactions were prepared by allylation of commercial diethyl malonate with allyl bromide and/or 3-chloro-2-methylpropene according to Hensle [54]. Their purity was estimated by ^1H NMR spectroscopy and found to be at least 95%. Other chemicals are commercially available and used as received. *N*-mesitylimidazole (**9**) was prepared according to the literature [47].

4.1.2. N-mesylimidazolium nitrate (*10*)

N-Mesitylimidazole **9** (250 mg, 1.34 mmol) was placed in a round bottom flask and cooled to 0 °C, next acetic anhydride (3.30 mL, 35 mmol) and fuming nitric acid (1.35 mL) were slowly added. The mixture was stirred at room temperature for 24 h. After this time it was concentrated to dryness in a stream of N_2. The residue was dissolved in a small volume of methylene chloride, and the product was precipitated with diethyl ether to give *N*-mesylimidazolium nitrate (**10**) (261 mg, 78% yield) as a white solid; M.p. 180 °C (with decomposition); IR (ATR) ν_{max} 3132, 1573, 1537, 1461, 1389, 1375, 1317, 833 cm^{-1}; ^1H NMR ($CDCl_3$, 400 MHz) δH 9.08 (1H, s, C2-H), 8.85 (1H, s, $CH_{imidazole}$), 7.15 (1H, s, $CH_{imidazole}$), 7.02 (2H, s, H-Ar), 2.34 (3H, s, *p*-CH_3), 2.03 (6H, s, 2x *o*-CH_3) ppm; ^{13}C NMR ($CDCl_3$, 100 MHz) δC 141.0, 136.6, 134.3, 130.8, 129.7, 122.1, 121.8, 21.0, 17.2; *m/z* (ESI) 187 ($[M\text{-}NO_3]^+$, 100%); HRMS (ESI): found 187.1235 $[C_{12}H_{15}N_2]^+$, requires 187.1230.

4.1.3. Catalyst *11*

A flame dried Schlenk flask with a magnetic stirring bar was charged under argon with catalyst **2** (120 mg, 0.2 mmol), nitrate **10** (50 mg, 0.2 mmol) and potassium *t*-butoxide (22 mg, 0.2 mmol). Next dry toluene (2 mL) was added. The reaction mixture turned green and was stirred at room temperature for 2 h. After this time the crude product was purified by column chromatography (CH_2Cl_2, then hexane – ethyl acetate *v/v* 1:2) to give catalyst **11** (89 mg, 55% yield) as a green solid; M.p. 163 °C; IR (ATR) ν_{max} 2919, 1586, 1466, 1375, 1231, 1112 cm^{-1}; ^1H NMR ($CDCl_3$, 400 MHz) δH 19.51 (1H, d, $J = 10.7$ Hz, Ru=CH), 9.13 (1H, d, $J = 6.8$ Hz, C2-H), 7.74 (1H, ddd, $J = 8.5$, 7.0, 1.4 Hz, H-Ar), 7.65 (1H, s, H-Ar), 7.12 (1H, t, $J = 7.6$ Hz, H-Ar), 6.94 (2H, d, $J = 3.2$ Hz, H-Ar), 6.87 (1H, d, $J = 8.2$ Hz, H-Ar), 6.78 (1H, s, H-Ar), 6.71 (1H, s, H-Ar), 4.75 (1H, sep, $J = 5.9$ Hz, -O-CH(CH_3)$_2$), 2.32 and 2.04–1.11 (48H, m, 3x CH_3-Mes + 3x Cy+(CH_3)$_2$CH-O-) ppm; ^{13}C NMR ($CDCl_3$, 100 MHz) δC 190.1, 171.1, 146.7, 146.6, 144.3, 139.9, 139.5, 135.7, 135.0, 133.6, 132.5, 129.1, 128.8, 122.4, 120.6, 114.0, 112.8, 69.9, 60.3, 35.7, 35.2, 34.9, 30.0, 29.0, 28.9, 28.8, 28.0, 27.9, 27.8, 27.8, 27.7, 27.7, 26.3, 22.4, 21.0, 17.4, 17.1, 17.0 ppm; *m/z* (ESI) 761 ($[M\text{-}(Cl^{\cdot}, OH^{\cdot})]^+$); HRMS(ESI): found 761.3271 $[C_{40}H_{58}N_3O_3P_{102}Ru]^+$, requires 761.3259. Crystals suitable for X-ray analysis were obtained by slow evaporation of a dichloromethane/hexane solution of the catalyst for 10 h in the refrigerator.

4.1.4. X-ray crystallographic data

$C_{40}H_{59}ClN_3O_4PRu$, green plates of 0.3 × 0.25 × 0.04 mm; monoclinic space group triclinic P1; a = 10.6421(3), b = 10.8897(3), c = 19.4405(6) Å; α = 78.883(3), β = 76.389(3), γ = 63.811(3)°; V = 1954.64 (12)Å^3; Z = 2; Dx = 1.382 Mg m^{-3}; μ(Cu Kα) = 4.60 mm^{-1}; 40133 reflections measured at SuperNova, Dual, Cu at home/near, Atlas diffractometer at 100K; 7660 reflections with $I > 2\sigma(I)$ were used for structure solution and refinement; data were corrected for numerical absorption using program CrysAlis PRO, SHELXL2016/6 [61]: $T_{min} = 0.252$, $T_{max} = 0.831$; R = 0.042; w*R* = 0.114.

CCDC 1556596 contains the supplementary crystallographic data for this compound. These data can be obtained free of charge from The Cambridge Crystallographic Data Centre via www.ccdc.cam.ac.uk/data_request/cif.

4.2. Theoretical calculations

Geometry optimization was performed using B3LYP [62] and TPSS functionals [59] with def2-SVP [62,63] basis set (def2-ECP for Ru atom) Grimme D3 [64] dispersion correction utilizing Turbomole V.7.1 [65]. All optimized structures were confirmed as local minima by the vibrational analysis [66]. The reaction energy barriers were calculated using the values of the total electronic energy correspondent to the fully optimized structures of reagents depicted in Scheme 5 and shown in *Supporting Information*. The free energy calculations, together with other thermodynamic functions (Tables S5–S6 in *Supporting Information*), were calculated from vibrational spectra using freeh module with scaling factor of 0.9614 (B3LYP) and 0.9914 (TPSS) in Turbomole V.7.1. The energy of coordination bond formation with nitrate, imidazole and chloride ligands was calculated using the single point calculations of the complex **11** with and without ligands. The absorption spectra were obtained using time-dependent DFT with the same set-up as above.

The discrete absorption peaks were broadened with the natural peak broadening using the convolution with Lorentzian profile. The visualization of the three-dimensional noncovalent interaction regions around the bond critical points of the π-interactions between the monomers of **11** in its dimer (Fig. 6) was made using the reduced density gradient, originated from the electron density and its first derivative [49,50]. The reduced density gradient was calculated using the promolecular densities of the complex **11** with NCIPLOT code (Version 3.0) [57,58]. *Ab initio* MD simulations were performed using PBE [67] functional with def2-SVP basis set and Grimme D3 dispersion correction. To optimize the computational set-up to investigate interactions between the dimer of complex **11** with ten HCl molecules, multipole-accelerated-resolution-of-identity method [68] was used and simulations for 2 ps at 800 K with the timestep of 8 a.u. using Nose-Hoover [69,70] thermostat were performed with Turbomole V.7.2.1. Three independent MD production runs were independently analyzed.

Acknowledgments

The authors acknowledge financial support from the National Science Centre, Poland (UMO-2015/17/N/ST5/03916). M. K. is grateful to M. Krstić for fruitful discussions. This work was performed on the computational resource ForHLR II funded by the Ministry of Science, Research and the Arts Baden-Württemberg and DFG ("Deutsche Forschungsgemeinschaft").

Appendix A. Supplementary data

Supplementary data to this article can be found online at https://doi.org/10.1016/j.jorganchem.2019.06.018.

References

[1] J.-E. Jee, J.L. Cheong, J. Lim, C. Chen, S.H. Hong, S.S. Lee, J. Org. Chem. 78 (7) (2013) 3048–3056.
[2] S.L. Mangold, R.H. Grubbs, Chem. Sci. 6 (8) (2015) 4561–4569.
[3] J.W. Morzycki, Steroids 76 (10) (2011) 949–966.
[4] M. Rössle, D.J. Del Valle, M.J. Krische, Org. Lett. 13 (6) (2011) 1482–1485.
[5] A. Fürstner, K. Radkowski, C. Wirtz, R. Goddard, C.W. Lehmann, R. Mynott, J. Am. Chem. Soc. 124 (24) (2002) 7061–7069.
[6] B.K. Keitz, K. Endo, P.R. Patel, M.B. Herbert, R.H. Grubbs, J. Am. Chem. Soc. 134 (1) (2012) 693–699.
[7] B.K. Keitz, K. Endo, M.B. Herbert, R.H. Grubbs, J. Am. Chem. Soc. 133 (25) (2011) 9686–9688.
[8] M.B. Herbert, R.H. Grubbs, Angew. Chem. Int. Ed. 54 (17) (2015) 5018–5024.
[9] M.J. Koh, T.T. Nguyen, J.K. Lam, S. Torker, J. Hyvl, R.R. Schrock, A.H. Hoveyda, Nature 542 (2017) 80–85.
[10] J. Tomasek, J. Schatz, Green Chem. 15 (9) (2013) 2317–2338.
[11] A. Kozłowska, M. Dranka, J. Zachara, E. Pump, C. Slugovc, K. Skowerski, K. Grela, Chem. Eur. J. 20 (43) (2014) 14120–14125.
[12] B.Ö. Öztürk, E. Bucak, S. Karabulut, J. Mol. Catal. A Chem. 376 (2013) 53–62.
[13] J.S.M. Samec, B.K. Keitz, R.H. Grubbs, J. Organomet. Chem. 695 (14) (2010) 1831–1837.
[14] B.Ö. Öztürk, B. Sariaslan, N.P. Bayramgil, S.K. Şehitoğlu, Appl. Catal. A Gen. 483 (2014) 19–24.
[15] B.Ö. Öztürk, A. Kolberg, S.K. Şehitoğlu, Macromol. Chem. Phys. 218 (9) (2017) 1600594.
[16] M.R. Buchmeiser, I. Ahmad, V. Gurram, P.S. Kumar, Macromolecules 44 (11) (2011) 4098–4106.
[17] M. Barbasiewicz, M. Malińska, K. Błocki, J. Organomet. Chem. 745–746 (2013) 8–11.
[18] A. Ben-Asuly, E. Tzur, C.E. Diesendruck, M. Sigalov, I. Goldberg, N.G. Lemcoff, Organometallics 27 (5) (2008) 811–813.
[19] A. Hryniewicka, J.W. Morzycki, S. Witkowski, J. Organomet. Chem. 695 (9) (2010) 1265–1270.
[20] A. Hejl, M.W. Day, R.H. Grubbs, Organometallics 25 (26) (2006) 6149–6154.
[21] R.M. Thomas, A. Fedorov, B.K. Keitz, R.H. Grubbs, Organometallics 30 (24) (2011) 6713–6717.
[22] A. Hafner, A. Mühlebach, P.A. van der Schaaf, Angew. Chem. Int. Ed. 36 (19) (1997) 2121–2124.
[23] A. Hafner, P.A. van der Schaaf, A. Mühlebach, Bernhard Paul, U. Schaedeli, T. Karlen, A. Ludi, Prog. Org. Coat. 32 (1) (1997) 89–96.
[24] T. Karlen, A. Ludi, A. Mühlebach, P. Bernhard, C. Pharisa, J. Polym. Sci. A Polym. Chem. 33 (10) (1995) 1665–1674.
[25] P.A. van der Schaaf, A. Hafner, A. Mühlebach, Angew. Chem. Int. Ed. 35 (16) (1996) 1845–1847.
[26] S. Rogalski, P. Żak, N. Tadeuszyk, K. Pyta, P. Przybylski, C. Pietraszuk, Dalton Trans. 46 (4) (2017) 1277–1282.
[27] S. Monsaert, A. Lozano Vila, R. Drozdzak, P. Van Der Voort, F. Verpoort, Chem. Soc. Rev. 38 (12) (2009) 3360–3372.
[28] H. Katayama, T. Yoshida, F. Ozawa, J. Organomet. Chem. 562 (2) (1998) 203–206.
[29] J. Wappel, R.C. Fischer, L. Cavallo, C. Slugovc, A. Poater, Beilstein J. Org. Chem. 12 (1) (2016) 154–165.
[30] B.K. Keitz, J. Bouffard, G. Bertrand, R.H. Grubbs, J. Am. Chem. Soc. 133 (22) (2011) 8498–8501.
[31] M. Rouen, P. Queval, L. Falivene, J. Allard, L. Toupet, C. Crévisy, F. Caijo, O. Baslé, L. Cavallo, M. Mauduit, Chem. Eur. J. 20 (42) (2014) 13716–13721.
[32] S. Monsaert, N. Ledoux, R. Drozdzak, F.J. Verpoort, Polym. Sci. A Polym. Chem. 48 (2) (2010) 302–310.
[33] T.E. Schmid, F. Modicom, A. Dumas, E. Borré, L. Toupet, O. Baslé, M. Mauduit, Beilstein J. Org. Chem. 11 (2015) 1541–1546.
[34] K. Voigtritter, S. Ghorai, B.H. Lipshutz, J. Org. Chem. 76 (11) (2011) 4697–4702.
[35] J. Patel, W.R. Jackson, A.K. Serelis, Inorg. Chim. Acta 357 (8) (2004) 2374–2378.
[36] C. Pietraszuk, S. Rogalski, B. Powała, M. Miętkiewski, M. Kubicki, G. Spólnik, W. Danikiewicz, K. Woźniak, A. Pazio, A. Szadkowska, et al., Chem. Eur. J. 18 (21) (2012) 6465–6469.
[37] M. Jawiczuk, A. Janaszkiewicz, B. Trzaskowski, Beilstein J. Org. Chem. 14 (1) (2018) 2872–2880.
[38] A. Zieliński, G. Szczepaniak, R. Gajda, K. Woźniak, B. Trzaskowski, D. Vidović, A. Kajetanowicz, K. Grela, Eur. J. Inorg. Chem. 2018 (32) (2018) 3675–3685.
[39] M. Karras, M. Dąbrowski, R. Pohl, J. Rybáček, J. Vacek, L. Bednárová, K. Grela, I. Starý, I.G. Stará, B. Schmidt, Chem. Eur. J. 24 (43) (2018) 10994–10998.
[40] C.K. Chu, T.-P. Lin, H. Shao, A.L. Liberman-Martin, P. Liu, R.H. Grubbs, J. Am. Chem. Soc. 140 (16) (2018) 5634–5643.
[41] A.D. Kulkarni, D.G. Truhlar, J. Chem. Theory Comput. 7 (7) (2011) 2325–2332.
[42] Y. Zhao, D.G. Truhlar, Chem. Phys. Lett. 502 (1) (2011) 1–13.
[43] I.C. Stewart, D. Benitez, D.J. O'Leary, E. Tkatchouk, M.W. Day, W.A. Goddard, R.H. Grubbs, J. Am. Chem. Soc. 131 (5) (2009) 1931–1938.
[44] D. Benitez, E. Tkatchouk, W.A. Goddard III, Chem. Commun. 46 (2008) 6194–6196.
[45] A. Poater, L.J. Cavallo, Mol. Catal. A: Chem. 324 (1) (2010) 75–79.
[46] A. Poater, E. Pump, S.V.C. Vummaleti, L. Cavallo, J. Chem. Theor. Comput. 10 (10) (2014) 4442–4448.
[47] G. Occhipinti, V.R. Jensen, K.W. Törnroos, N.Å. Frøystein, H.-R. Bjørsvik, Tetrahedron 65 (34) (2009) 7186–7194.
[48] M.R.M. Domingues, M.G.O. S.-Marques, P. Domingues, M.G. Neves, J.A.S. Cavaleiro, A.J. Ferrer-Correia, O.V. Nemirovskiy, M.L. Gross, J. Am. Soc. Mass. Spectrom. 12 (4) (2001) 381–384.
[49] S.H. Hong, A.G. Wenzel, T.T. Salguero, M.W. Day, R.H. Grubbs, J. Am. Chem. Soc. 129 (25) (2007) 7961–7968.
[50] E.M. Leitao, S.R. Dubberley, W.E. Piers, Q. Wu, R. McDonald, Chem. Eur. J. 14 (2008) 11565–11572.
[51] K. Vehlow, S. Gessler, S. Blechert, Angew. Chem. Int. Ed. 46 (2007) 8082–8085.
[52] J. Mathew, N. Koga, Ch. H. Suresh, Organometallics 27 (2008) 4666–4670.
[53] S. Hong, A. Chlenov, M. Day, R. Grubbs, Angew. Chem. Int. Ed. 46 (2007) 5148–5151.
[54] M.B. Dinger, J.C. Mol, Organometallics 22 (5) (2003) 1089–1095.
[55] M. Dinger, J. Mol, Eur. J. Inorg. Chem. (2003) 2827–2833.
[56] E.R. Johnson, S. Keinan, P. Mori-Sánchez, J. Contreras-García, A.J. Cohen, W. Yang, J. Am. Chem. Soc. 132 (18) (2010) 6498–6506.
[57] J. Contreras-García, E.R. Johnson, S. Keinan, R. Chaudret, J.-P. Piquemal, D.N. Beratan, W. Yang, J. Chem. Theor. Comput. 7 (3) (2011) 625–632.
[58] E. Arunan, G.R. Desiraju, R.A. Klein, J. Sadlej, S. Scheiner, I. Alkorta, D.C. Clary, R.H. Crabtree, J.J. Dannenberg, P. Hobza, H.G. Kjaergaard, A.C. Legon, B. Mennucci, D.J. Nesbitt, Pure Appl. Chem. 83 (2011) 1619–1636.
[59] J. Tao, J.P. Perdew, V.N. Staroverov, G.E. Scuseria, Phys. Rev. Lett. 91 (14) (2003) 146401.
[60] Y. Kanai, X. Wang, A. Selloni, R. Car, J. Chem. Phys. 125 (23) (2006) 234104.
[61] E.M. Hensle, J. Tobis, J.C. Tiller, W. Bannwarth, J. Fluorine Chem. 129 (10) (2008) 968–973.
[62] A.D. Becke, J. Chem. Phys. 96 (3) (1992) 2155–2160.
[63] A. Schäfer, H. Horn, R. Ahlrichs, J. Chem. Phys. 97 (4) (1992) 2571–2577.
[64] S. Grimme, J. Antony, S. Ehrlich, H. Krieg, J. Chem. Phys. 132 (15) (2010) 154104.
[65] R. Ahlrichs, M. Bär, M. Häser, H. Horn, C. Kölmel, Chem. Phys. Lett. 162 (3) (1989) 165–169.
[66] P. Deglmann, F. Furche, J. Chem. Phys. 117 (21) (2002) 9535–9538.
[67] J.P. Perdew, K. Burke, M. Ernzerhof, Phys. Rev. Lett. 77 (18) (1996) 3865–3868.
[68] M. Von Arnim, R. Ahlrichs, J. Comput. Chem. 19 (15) (1998) 1746–1757.
[69] S.A. Nosé, J. Chem. Phys. 81 (1) (1984) 511–519.
[70] W.G. Hoover, Phys. Rev. A 31 (3) (1985) 1695–1697.